

# The unexpectedly large dust and gas content of quiescent galaxies at $z > 1.4$

R. Gobat<sup>1\*</sup>, E. Daddi<sup>2</sup>, G. Magdis<sup>3,4</sup>, F. Bournaud<sup>2</sup>, M. Sargent<sup>5</sup>, M. Martig<sup>6</sup>, S. Jin<sup>2,7</sup>, A. Finoguenov<sup>8,9</sup>, M. Béthermin<sup>10</sup>, H. S. Hwang<sup>1</sup>, A. Renzini<sup>11</sup>, G. W. Wilson<sup>12</sup>, I. Aretxaga<sup>13</sup>, M. Yun<sup>12</sup>, V. Strazzullo<sup>14</sup> and F. Valentino<sup>3</sup>

**Early-type galaxies (ETGs) contain most of the stars present in the local Universe and, above a stellar mass content of  $\sim 5 \times 10^{10}$  solar masses, vastly outnumber spiral galaxies such as the Milky Way. These massive spheroidal galaxies have, in the present day, very little gas or dust in proportion to their mass<sup>1</sup>, and their stellar populations have been evolving passively for over 10 billion years. The physical mechanisms that led to the termination of star formation in these galaxies and depletion of their interstellar medium remain largely conjectural. In particular, there are currently no direct measurements of the amount of residual gas that might still be present in newly quiescent spheroidals at high redshift<sup>2</sup>. Here we show that quiescent ETGs at redshift  $z \sim 1.8$ , close to their epoch of quenching, contained at least two orders of magnitude more dust at a fixed stellar mass compared with local ETGs. This implies the presence of substantial amounts of gas (5–10%), which has been consumed less efficiently than in more active galaxies, probably due to their spheroidal morphology, consistent with our simulations. This lower star formation efficiency, combined with an extended hot gas halo possibly maintained by persistent feedback from an active galactic nucleus, keep ETGs mostly passive throughout cosmic time.**

The presence of quiescent galaxies, with very low relative star formation rates (SFRs), has been established up to  $z \sim 3$  (refs<sup>3,4</sup>). Their existence a mere 2 Gyr after the Big Bang implies that, in at least some regions of the Universe, the processes responsible for the cessation of star formation were already very efficient. The termination of star formation in ETGs is usually attributed to the removal of cool gas reservoirs (for example, by stellar or quasar feedback<sup>5</sup>) and/or to the suppression of gas infall and cooling (such as by virial shocks or active galactic nucleus (AGN) feedback<sup>6,7</sup>). Alternatively, the growth of bulges and stellar spheroids is thought to stabilize gas reservoirs, making star formation inefficient compared with disk galaxies<sup>8,9</sup>. If the latter plays an important role in galaxy quenching, we might expect substantial reservoirs of untapped gas to exist in galaxies that have recently turned quiescent. However, detecting this residual gas at high redshift, close to the epoch of quenching for massive quiescent galaxies, is very challenging<sup>2</sup>, and all attempts have so far been unsuccessful.

Deep survey fields allow us to circumnavigate this issue. By combining data from large numbers of undetected quiescent galaxies, their average far-infrared (FIR) emission can be observed, which traces the cold dust present in their interstellar medium (ISM) and, indirectly, their SFR. We select 977 isolated, high-mass (median stellar mass  $\langle M_{\star} \rangle = 1.1 \times 10^{11} M_{\odot}$ ) quiescent galaxies in the 2 square degree Cosmic Evolution Survey (COSMOS) field by combining two different photometric criteria (BzK<sup>10</sup> and UVJ<sup>11</sup>, where B, z, K, U, V and J are photometric bands) and keeping only objects that are individually undetected at observed mid-infrared (MIR) wavelengths (Methods). These criteria ensure that the sample contains only the least star-forming galaxies at  $z = 1.4$ – $2.5$ , with clear early-type morphologies (as implied by a high median Sérsic index  $n \sim 3.5$ ; Methods). We extract cutouts centred at the position of each galaxy from the 24  $\mu\text{m}$  (MIR), 100–500  $\mu\text{m}$  (FIR), 0.85–1.1 mm (submillimetre) and 10–20 cm (radio) observations of the COSMOS, and perform a median stacking analysis at each wavelength. After correcting for the contribution from satellite galaxies and unassociated neighbours in the line of sight (Methods), we obtain a clean measure of the FIR and radio emission of the quiescent galaxies, with detections in all but two bands (100  $\mu\text{m}$  and 160  $\mu\text{m}$ ) ranging in significance from  $3.5\sigma$  to  $11.9\sigma$  (Fig. 1).

We model both the FIR emission from cold dust<sup>12</sup> and the non-thermal radio emission from star formation, based on the FIR flux (Methods). Although the models underpredict the observed radio fluxes by a factor of  $\sim 3$  (corresponding to an excess of  $\sim 5 \times 10^{22} \text{ W Hz}^{-1}$ ), they reproduce the FIR spectral energy distribution (SED) well, implying a total infrared luminosity  $L_{\text{IR}} = 2.9 \pm 0.9 \times 10^{10} L_{\odot}$ . Furthermore, sampling the peak ( $\sim 150 \mu\text{m}$  rest frame) and Rayleigh–Jeans tail ( $> 400 \mu\text{m}$  rest frame; Fig. 1) of the FIR emission allows for an accurate determination of the dust temperature,  $T_{\text{dust}} \sim 21$ – $25 \text{ K}$ , and dust mass,  $M_{\text{dust}} = 1_{-0.4}^{+0.6} \times 10^8 M_{\odot}$ . The temperature of the cold dust component, as suggested by the lack of detection at  $\sim 100$ – $160 \mu\text{m}$  but not at  $\geq 250 \mu\text{m}$ , is similarly up to 10 K lower than that of the main sequence of star formation (MS) at the same  $L_{\text{IR}}$  (ref. 13), among the lowest values for star-forming galaxies at any redshift but consistent with that of local ETGs<sup>14</sup>. This low temperature also confirms that the measured FIR emission does not originate from star-forming satellites, which would

<sup>1</sup>School of Physics, Korea Institute for Advanced Study, Seoul, Republic of Korea. <sup>2</sup>CEA, IRFU, DAp, AIM, Université Paris-Saclay, Université Paris Diderot, Sorbonne Paris Cité, CNRS, Gif-sur-Yvette, France. <sup>3</sup>Dark Cosmology Centre, Niels Bohr Institute, University of Copenhagen, Copenhagen, Denmark.

<sup>4</sup>Institute for Astronomy, Astrophysics, Space Applications and Remote Sensing, National Observatory of Athens, Athens, Greece. <sup>5</sup>Astronomy Centre, Department of Physics and Astronomy, University of Sussex, Brighton, UK. <sup>6</sup>Astrophysics Research Institute, Liverpool John Moores University, Liverpool, UK. <sup>7</sup>School of Astronomy and Space Science, Nanjing University, Nanjing, China. <sup>8</sup>Max-Planck-Institute for Extraterrestrial Physics, Garching, Germany.

<sup>9</sup>Department of Physics, University of Helsinki, Helsinki, Finland. <sup>10</sup>CNRS, LAM (Laboratoire d'Astrophysique de Marseille) UMR 7326, Aix Marseille Univ., Marseille, France. <sup>11</sup>INAF-Osservatorio Astronomico di Padova, Padua, Italy. <sup>12</sup>Department of Astronomy, University of Massachusetts, Amherst, MA, USA.

<sup>13</sup>Instituto Nacional de Astrofísica, Óptica y Electrónica (INAOE), Puebla, Mexico. <sup>14</sup>Department of Physics, Ludwig-Maximilians-Universität, Munich, Germany.

\*e-mail: [rgobat@kias.re.kr](mailto:rgobat@kias.re.kr)

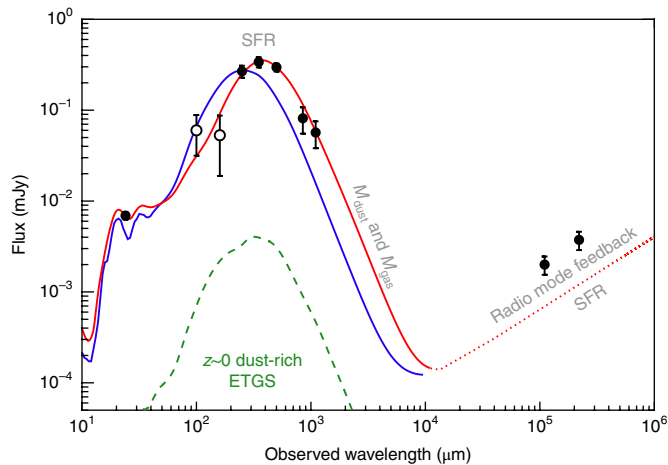


**Fig. 1 | Mid-infrared to radio SED of 24  $\mu\text{m}$ -undetected BzK + UVJ-selected passive galaxies.** Stacked cutout images are used (filled circles; open circles represent  $<3\sigma$  non-detections), with best-fit model from Draine and Li<sup>12</sup> (solid red curve, dotted when extended into the radio regime; Methods). For comparison, the ‘best-fit’ standard MS template<sup>15</sup>, which has hotter dust, is shown in blue, and the median best-fit dust component to the FIR SED of local dust-rich ETGs is the dashed green curve. The latter model has been redshifted to  $z = 1.76$  and rescaled to the same stellar mass. All models have been broadened using the redshift distribution of the sample as kernel. The error bars on the MIR, FIR and radio fluxes show the bootstrap uncertainties derived from the stack.

have  $T_{\text{dust}}$  values closer to those of the MS ( $T_{\text{dust,MS}} \sim 30 \text{ K}$ ; Methods). These distant ETGs appear, however, to be much more dust rich than their local counterparts, with  $(M_{\text{dust}}/M_{\star})_{z=1.76} \sim 8 \times 10^{-4}$ , where  $M_{\star}$  is stellar mass, compared with  $(M_{\text{dust}}/M_{\star})_{z=0} \sim 10^{-6} - 10^{-5}$  locally<sup>1,14</sup>, a difference of  $\gtrsim 2$  orders of magnitude. We convert the measured dust mass into a gas mass assuming a gas-phase metallicity close to the solar value and a metallicity-dependent gas-to-dust ratio (G/D)<sup>15</sup>, which yields  $M_{\text{gas}} = 9.5^{+5.6}_{-3.5} \times 10^9 M_{\odot}$  (Methods). In nearby quiescent galaxies for which such measures exist, the relative mass of molecular ( $\text{H}_2$ ) to atomic (HI) hydrogen gas is in the range  $M(\text{H}_2)/M(\text{HI}) \sim 0.1 - 100$ , with molecular gas nevertheless dominating by a factor of  $\sim 5$  on average<sup>16,17</sup>. We thus assume that distant quiescent galaxies are similar to their local counterparts in this regard (Methods) and that  $M_{\text{gas}}$  hereafter refers to molecular hydrogen rather than the combined HI and  $\text{H}_2$  gas mass.

The large amount of dust we detect, and the inferred gas mass, imply that high-redshift ETGs are remarkably gas rich, with up to 11% of their baryonic mass being in the form of gas. As with the dust fraction, this represents an increase of more than two orders of magnitude with respect to the local Universe<sup>1</sup> (Fig. 2), even when accounting for differences in stellar mass between local and high-redshift samples, and a cosmic evolution that vastly exceeds the similar increase in the gas fraction of star-forming galaxies. In ‘normal’ star-forming galaxies, the FIR and submillimetre emission is a relatively pure tracer of star formation. If the observed cold dust emission does indeed arise from star formation activity, converting<sup>18</sup>  $L_{\text{IR}}$  into a SFR then yields  $4.8^{+1.8}_{-1.3} M_{\odot} \text{ yr}^{-1}$ , in excellent agreement with the SFR of  $z \sim 1.5$  ETGs derived from optical spectroscopic diagnostics<sup>19</sup>, which probe different timescales (a few tens of million years for spectroscopic line emission, several times that for FIR emission). Given the large stellar mass of these galaxies, it implies that the distant ETGs have a specific SFR (sSFR) that is a factor of  $\sim 30$  lower than that of active galaxies on the MS at the same epoch (Fig. 3). The presence of both such large gas reservoirs and low SFR would imply that the star formation efficiency (SFE) of these quiescent galaxies

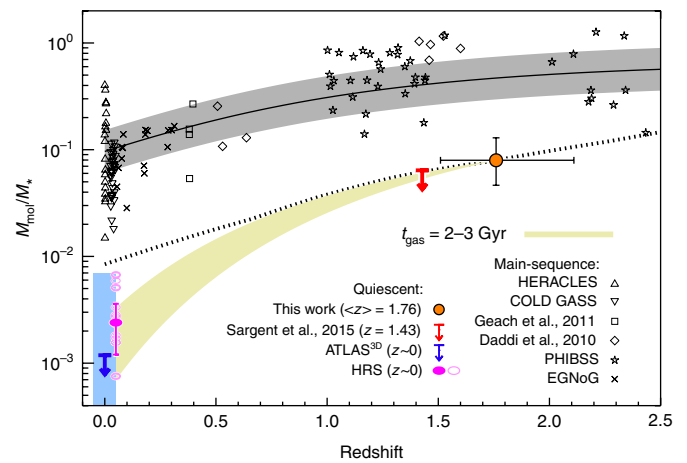


**Fig. 2 | Evolution of the molecular gas fraction  $M_{\text{mol}}/M_{\star}$  as a function of redshift for both quiescent and MS galaxies.** The latter include low-redshift<sup>97,98</sup>, intermediate-redshift<sup>99,100</sup> and  $z > 1$  MS galaxies<sup>15,101,102</sup>. The distant ETG sample is shown as the orange filled circle, with error bars from the SED modelling (Methods), and the upper-limit constraints from CO( $J = 2 - 1$ ) observations of a massive ETG at a similar redshift<sup>2</sup> are shown as the red arrow. The blue arrow marks the median upper limit on this ratio for ETGs in the ATLAS<sup>3D</sup> survey, with the light blue shaded region showing the range of values for the detected subsample (22%) of ATLAS<sup>3D</sup>. For comparison, local ETGs in the Herschel Reference Survey (HRS) are shown as magenta ellipses: open for gas masses from CO measurements<sup>103</sup>, including upper limits, and filled for dust masses<sup>103</sup> converted using the same G/D, with the error bar showing the median absolute deviation of the sample. The black curve and grey strip, respectively, show the evolution of an average MS galaxy<sup>104</sup> with stellar mass  $5 \times 10^{10} M_{\odot}$ , and a 0.2 dex scatter approximately corresponding to the  $1\sigma$  scatter of the MS. The dotted line shows the relation<sup>104</sup> offset by a factor of  $-6$  and for a stellar mass of  $\log M^*(z) + \Delta M$ , where  $\Delta M$  is the offset between the median mass of the total pBzK + UVJp sample and the characteristic mass  $M^*$  of the stellar mass function of quiescent galaxies at the median redshift of the sample. Finally, the green-yellow region shows gas consumption in the closed-box case (no gas inflow or outflow), with a timescale  $t_{\text{gas}}$  between 2 Gyr and 3 Gyr (lower and upper edge, respectively). ‘PHIBSS’ is the Institut de Radioastronomie Millimétrique Plateau de Bure High- $z$  Blue Sequence Survey, ‘EGNoG’ is the Evolution of Molecular Gas in Normal Galaxies survey, ‘COLD GASS’ is the CO Legacy Database for the Galaxy Evolution Explorer Arecibo Sloan Digital Sky Survey and ‘HERACLES’ is the Heterodyne Receiver Array CO-Line Extragalactic Survey.

is 2–3 times lower than that of disk galaxies and comparable to that of local ETGs<sup>20</sup> (Fig. 3). This value is conservative and thus could be even lower, if part of the FIR emission of these distant ETGs arises from, for example, heating of cirrus dust by an evolved stellar population consistent with the median ETG age at this redshift. Whether massive, main-sequence stars or postmain-sequence stars (ongoing or past star formation, respectively) are the dominant heating source of the dust in these ETGs then depends on its spatial distribution (that is, concentrated in and around molecular clouds or diffuse), which is still unknown. The good agreement between optical and infrared-based SFRs<sup>19</sup>, however, suggests that residual star formation is an important contributing mechanism to the FIR emission. A low SFE is also consistent with the low dust temperature and small value of the dust-mass weighted luminosity  $\langle U \rangle$  estimated from the infrared SED, since the intensity of the radiation field can be related to the SFE and metallicity  $Z$  by the relation  $\langle U \rangle \propto \text{SFE}/Z$  (ref. 15). It also implies a longer gas consumption timescale,  $t_{\text{gas}} = 2 - 3 \text{ Gyr}$ , compared with  $\lesssim 1 \text{ Gyr}$  for MS galaxies. A low efficiency in ETGs

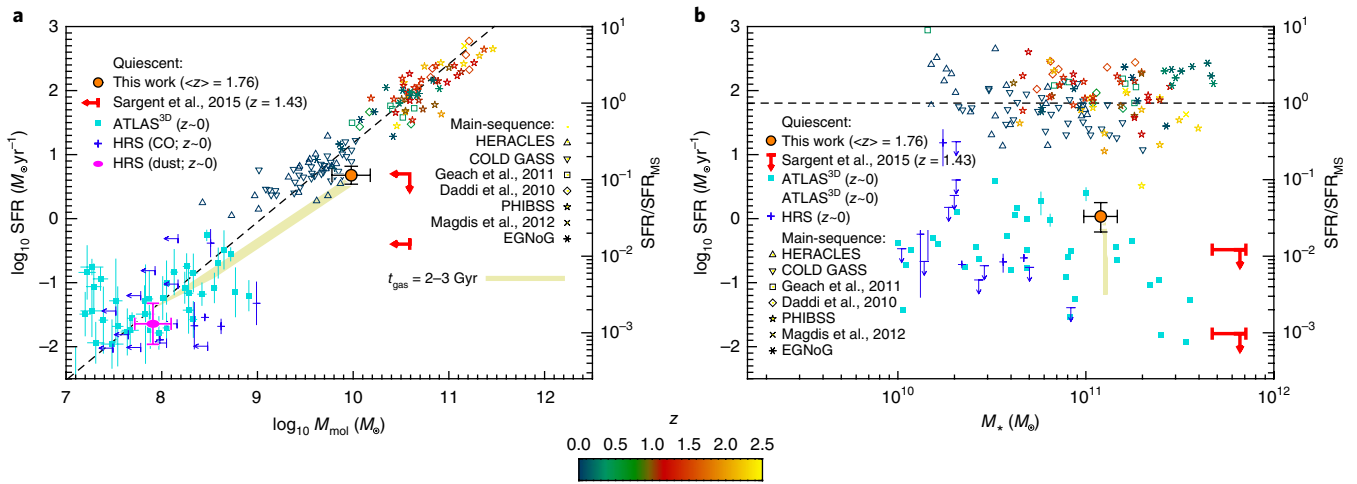


**Fig. 3 | Galactic SFRs.** **a**, Correlation between the molecular gas content and SFR of galaxies, including the same MS samples as in Fig. 2. Our median measurement, shown as an orange filled circle with error bars (Methods), is offset by  $\sim 3\sigma$  from the average SFR– $M_{\text{mol}}$  relation for MS galaxies<sup>104</sup> (black dashed line). For comparison, the upper-limit constraints from CO(2–1) observations of a massive ETG at a similar redshift<sup>3</sup> are shown as red arrows, local ETGs from the HRS<sup>103</sup> as dark blue crosses and arrows (in the case of upper limits on  $M_{\text{mol}}$ ), and independent measurements from the local ATLAS3D sample<sup>16,105</sup>, when more than 1 dex below the MS in the SFR, as light blue squares. The average SFR and dust-derived gas mass of HRS ETGs is shown as a filled magenta ellipse, with error bars showing the median absolute deviation of the sample. The green-yellow region shows the same closed-box evolution from  $z=1.76$  to  $z=0$  as in Fig. 2. **b**, The SFR of star-forming and quiescent galaxies as a fraction of the MS one<sup>104</sup>, for the same data as in **a**.

is predicted by high-resolution hydrodynamical simulations<sup>8,21</sup> (Methods), in which the SFE of a forming ETG, which starts as a high-redshift disk galaxy, decreases by a factor of 5–10 when the gas drops below a critical value (Fig. 4). In our simulations of gas disks embedded in spheroids, this corresponds to a gas fraction of 20–25%. This effect is linked to the presence of the spheroidal stellar component, which, unlike a stellar disk, does not destabilize the gas disk. Conversely, in galaxies containing more than  $\sim 25\%$  of gas, regardless of their stellar structure, the gas remains unstable and capable of forming stars efficiently.

Our observations suggest that this process does indeed occur in high-redshift ETGs when the gas fraction has been reduced enough, and that the suppression of star formation thus does not require the complete removal of cool gas reservoirs. In principle, a passive evolution with no further accretion and a low SFE could then account for the low gas fractions of local ETGs, compared with their high-redshift counterparts, while increasing their stellar mass by only a small fraction between  $z \sim 1.76$  and  $z=0$  (Fig. 2). However, gas in local ETGs has probably had a more complex history. Indeed, several channels exist through which these galaxies could have been replenished with gas. Given ETG ages of  $<3 \text{ Gyr}$  inferred from spectroscopy<sup>19</sup>, we can estimate that  $\sim 4.5 \times 10^{10} M_{\odot}$  of metal-enriched gas was already returned to the ISM by stellar evolution, at a rate of  $\lesssim 2.9 M_{\odot} \text{yr}^{-1}$  at  $z=1.76$ , with another  $\sim 10^{10} M_{\odot}$  produced over the next 10 Gyr assuming passive evolution (Methods). Gas is also expected to be reaccreted through mergers with gas-rich satellite galaxies and through the cosmic web. This suggests that there must exist other processes to keep the cold gas fraction low in these ETGs for the rest of their cosmic evolution, either by efficiently removing the surplus gas or by preventing it from cooling. There are three such probable ‘maintenance’ mechanisms: first, the host halos of these distant ETGs are, at  $\gtrsim 10^{13} M_{\odot}$ , already massive enough to support a hot atmosphere, as evidenced by X-ray stacking (Methods). This hot gas can efficiently prevent the infall of cold gas onto the central galaxy<sup>6</sup>. The X-rays emitted by the halo can also remove, on short timescales and through sputtering, the dust produced by stellar evolution, thus contributing to the evolution of the dust content of ETGs between  $z > 1.4$  and  $z=0$  (Methods). Second, the ‘radio-mode’

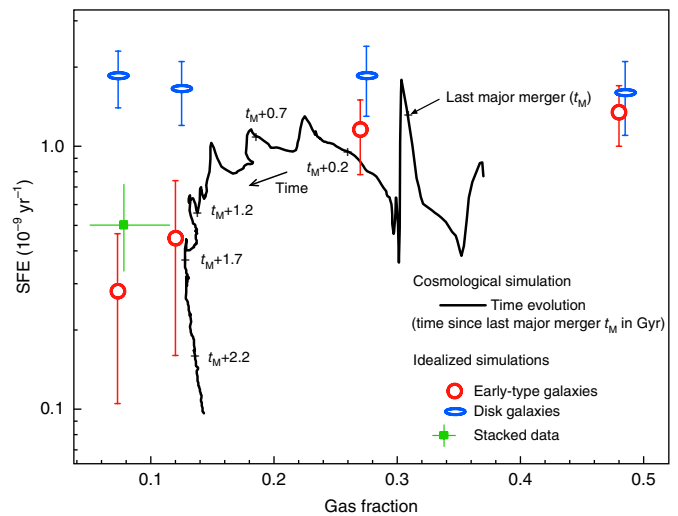


**Fig. 4 | SFE as a function of gas fraction in high-resolution hydrodynamic simulations.** The black line shows the evolutionary track of an ETG with an embedded gas disk in a cosmological zoom-in simulation, with initial peaks of SFE corresponding to galaxy mergers, followed by gas consumption and a strong decrease of the SFE when the gas fraction becomes lower than 20–25%. This effect, which has been dubbed ‘morphological quenching’, does not occur in galaxies whose stellar structure remains disk-like<sup>8</sup>. The galaxy already has an ETG morphology at the beginning of the track (Methods), but quenches  $\sim 2 \text{ Gyr}$  later only when enough gas has been consumed. The red and blue symbols are from idealized simulations of galaxies of ETG and disk-dominated galaxies, respectively, where both gas structure and star formation are resolved at the parsec scale<sup>87</sup> (Methods). The error bars correspond to the root mean squared fluctuation of the SFE between various snapshots of a given simulation. These confirm that the SFE drops below gas fractions of 20–25% only for ETGs, at a level consistent with our observations (filled green square with error bars). Local ETGs from ATLAS<sup>3D</sup> and HRS have SFEs similar to the idealized simulations and high-redshift sample, but with much lower gas fractions ( $3 \times 10^{-3}$  on average).

feedback from AGN-driven jets (as tantalizingly suggested by the systematic radio excess, which would imply a duty cycle of nearly 100%, as opposed to 1% locally; Fig. 1 and Methods) can not only heat the halo gas but also regularly drive away a fraction of the cold gas reservoir<sup>7</sup>. Finally, gravitational interaction between satellites and the halo can also provide a source of heating for the gas<sup>22</sup>.

The large amounts of dust we detect in our  $z > 1.4$  sample, through its FIR emission, implies similarly large quantities of molecular hydrogen. This  $H_2$  gas would thus appear to be abundant enough in these galaxies to be detectable with the Atacama Large Millimeter Array through submillimetre line tracers, although the confirmation of even a single galaxy can be expected to require several hours of observation. Nevertheless, our result indicates that semidirect studies of gas in high-redshift quiescent galaxies are already feasible, although the large time expenditure required and still-unknown dependencies of the dust and gas fractions on stellar mass or on the environment could make their design challenging.

## Methods

**Conventions.** Stellar masses and SFRs derived from photometry assume a Salpeter<sup>23</sup> stellar initial mass function (IMF), in accordance with the literature on IMF variations in ETGs<sup>24–26</sup>. We assume for consistency the same IMF for galaxies on the MS. For distances, cosmic times and cosmological simulations, we assume a  $\Lambda$ CDM cosmology, with  $H_0 = 70 \text{ km s}^{-1} \text{ Mpc}^{-1}$ ,  $\Omega_M = 0.3$  and  $\Omega_\Lambda = 0.7$  (refs<sup>27,28</sup>).

**Sample selection.** We select galaxies from the COSMOS field<sup>29</sup> using public ultraviolet-to-near-infrared photometry<sup>30,31</sup> and a new point-source-matched catalogue (Jin, S. et al., manuscript in preparation;  $8 \mu\text{Jy}$  r.m.s. sensitivity) based on public MIPS (Multiband Imaging Photometer for Spitzer)  $24 \mu\text{m}$  data<sup>32</sup>. We use spectroscopic redshifts from the zCOSMOS survey<sup>33</sup> when available, and photometric redshifts<sup>31,32</sup> otherwise. Quiescent galaxies at  $1.4 < z < 2.5$  are first selected using the BzK criterion<sup>10</sup>, using photometry from the original 2010 catalogue<sup>30</sup>, for which colour selections have been extensively tested. However, the rest of the analysis makes use of more recent UltraVISTA (Deep Survey with the Visible and Infrared Survey Telescope for Astronomy) photometry<sup>31</sup>. In this first step, galaxies undetected at  $< 3\sigma$  in the B band, implying a  $B - z$  colour compatible with the locus of quiescent galaxies, are also considered. Photometric redshifts calibrated for passive stellar populations<sup>34</sup> are then used to compute rest-frame U-, V- and J-band magnitudes for the initial sample, so as to discard from the sample those galaxies that are not also selected as quiescent by the high-redshift UVJ criterion<sup>35</sup>. As illustrated in Supplementary Fig. 1, this double selection minimizes the number of interlopers due to photometric uncertainties and highly reddened star-forming galaxies. We then discard from the sample those sources that are detected at  $\geq 3\sigma$  significance in the  $24 \mu\text{m}$  catalogue, about 14% of the sample, as it implies either considerable star formation or AGN activity. We then keep only galaxies with stellar masses higher than  $\log M_* = 10.8 M_\odot$ , within uncertainties, so as to ensure that the stellar mass distribution of this sample is similar to that of a spectroscopically observed subsample<sup>19</sup> (Supplementary Fig. 2) for which accurate redshifts and stellar population parameters (age, SFR, metallicity) were estimated. This mass limit also corresponds to twice the completeness limit of the catalogue for  $z > 1.5$  quiescent galaxies<sup>36</sup>. We also ignore possible galaxy pairs, that is, with concordant redshifts (within  $\Delta z_{\text{phot}} \leq 0.2$ , where  $\Delta z_{\text{phot}}$  is the absolute difference between the photometric redshifts of the two galaxies in the possible pair) and separated by less than  $60''$  ( $\leq 30\%$  of the sample), to simplify the modelling of the FIR emission (Supplementary Section 3). The final sample contains 977 passive galaxies selected from a combined BzK + UVJ diagram, with a median redshift  $\langle z \rangle = 1.76$  and a median stellar mass  $\langle M_* \rangle = 1.1 \times 10^{11} M_\odot$ .

**FIR stack.** The COSMOS includes imaging data at  $24 \mu\text{m}$  (MIPS<sup>32</sup>),  $100 \mu\text{m}$  and  $160 \mu\text{m}$  (Herschel/PACS (Photodetecting Array Camera and Spectrometer), from the PEP (PACS Evolutionary Probe) survey<sup>37</sup>),  $250 \mu\text{m}$ ,  $350 \mu\text{m}$  and  $500 \mu\text{m}$  (Herschel/SPIRE (Spectral and Photometric Imaging Receiver), from the HerMES (Herschel Multi-tiered Extragalactic Survey)<sup>38</sup>),  $850 \mu\text{m}$  (James Clerk Maxwell Telescope/SCUBA-2 (Submillimetre Common-User Bolometer Array 2)<sup>39</sup>),  $1.1 \text{ mm}$  (Atacama Submillimetre Telescope Experiment/AzTEC (Astronomical Thermal Emission Camera)<sup>40</sup>),  $3 \text{ GHz}$  (ref.<sup>41</sup>) and  $1.4 \text{ GHz}$  (ref.<sup>42</sup>) (VLA (Very Large Array)). From these data, we extract cutouts centred on each source in the sample with sizes five times larger than the beam full-width at half-maximum. These are then combined to create a median two-dimensional image in each band (Supplementary Fig. 3), using 1,000 bootstrap resamplings of the data with sizes of half the initial sample to estimate the variance of the sample. At each bootstrap iteration, we estimate the flux of the central ETG by assuming that the resulting median image is produced by a combination of point-like emission, contribution from star-forming satellites and a background term. The FIR emission from the ETGs' satellite halos is estimated in the following way<sup>36</sup>: we select, within  $120''$  of

each ETG (hereafter, 'central'), star-forming galaxies that satisfy the high-redshift UVJ criterion<sup>35</sup> and with  $z_{1.68} < z_{\text{cen}} < z_{1168}$ , where  $z_{\text{cen}}$  is the redshift of the central, and  $z_{1.68}$  and  $z_{1168}$  are the lower and upper, respectively, 68% confidence limit to the photometric redshift of the putative satellites. Subtracting the background distribution<sup>36</sup> yields an excess of 1,234 star-forming satellites, with an additional  $\sim 400$  quiescent ones, corresponding to an average of 1–2 satellites per central and a stellar mass distribution consistent with field BzK-selected galaxies. As shown in Supplementary Fig. 4, the resulting overdensity of star-forming satellite galaxies (hereafter, 'satellite halo') becomes clear when averaging over the whole sample and reaches the level of the background at  $\geq 30''$  from the central. We estimate the SFR of each satellite thus selected by modelling its rest-frame ultraviolet (UV) SED with constant star formation stellar population models<sup>43</sup>, with and without dust extinction<sup>44</sup>. The obscured SFR of satellites is then given by the difference between the dust-corrected and uncorrected UV SFRs. We then divide the field around the centrals in annuli of width  $\Delta \log r = 0.1''$ , starting at  $r = 1''$  from the central (that is, twice the seeing and more than six times the galaxies' effective radius; Supplementary Section 4), and sum in each annulus the obscured SFR of satellites to estimate the radial SFR surface density profile of the satellite halo. We model this profile using a combination of a  $\beta$  function and a multiplicative, two-parameter 'quenching' term of the form  $\min(r/r_q, 1)^{\alpha_q}$  (Supplementary Fig. 4b), where  $r$  is the distance to the central, and  $r_q$  and  $\alpha_q$  are free parameters, and extrapolate it to the central  $2''$ . As the formal error on these parameters contributes negligibly to the uncertainty budget, we fix them to their best-fit values. As the obscured SFR is linearly proportional to the infrared luminosity, the SFR surface density profile is then used as a model of the FIR emission of satellites. Quiescent satellites are not included in this estimate because their average number and stellar mass densities are low, and amount to  $(6 \pm 0.7) \times 10^9 M_\odot$  when integrated up to the virial radius. If the mass fraction and temperature of the dust in quiescent satellites are the same as for the quiescent centrals (see below), their contribution to the FIR emission is at most 5%, that is, smaller than the uncertainties. This value could be even lower if, conversely, the quenching of star formation in these satellites was mediated by mechanisms that removed the ISM at a greater rate than for the centrals.

When the full-width at half-maximum of the FIR instrumental beam is smaller than the extension of the satellite halo ( $\sim 20''$ ; this applies to the MIPS, PACS,  $250 \mu\text{m}$  SPIRE, SCUBA-2, AzTEC and VLA data), the FIR flux of the central in each band is estimated from the decomposition of the observed signal into a point source and a two-dimensional extended component based on the SFR profile of the satellite halo, convolved with the instrumental beam. Conversely, the beam size of SPIRE at  $350 \mu\text{m}$  and  $500 \mu\text{m}$  is larger than the extent of the satellite halo, precluding a decomposition of the stacked cutout image into two components. In this case, we fit only the central part of the cutout (within one beam full-width at half-maximum) with a single point source, and correct the estimate for the fraction of flux in the beam arising from the satellite halo, assuming a main-sequence FIR SED<sup>15</sup> for the latter. In the bands where the two-component decomposition is possible, the two methods yield consistent flux estimates. In both cases, the flux of the central galaxy is essentially measured through a point source fit to the unconvolved image. We then take the variance of bootstrap iterations as uncertainty on the flux. Finally, the measured fluxes are corrected for clustering of randomly distributed sources, based on simulations performed on the FIR COSMOS data<sup>45</sup>. The clustering-corrected fluxes and satellite corrections are given in Supplementary Table 1. These, and the total infrared luminosity  $L_{\text{IR}}$  that we find, are a factor of  $\sim 5$  lower than those inferred recently for quiescent galaxies at similar redshift and stellar mass<sup>46</sup>, but without probing the Rayleigh–Jeans tail of the cold dust emission. Likewise, the recovered  $1.1 \text{ mm}$  is a factor of  $\sim 4$  lower than the contribution of quiescent galaxies to the cosmic infrared background<sup>47</sup>. However, both analyses use a different selection criterion, which, along with our strict treatment of satellite emission, could account for this difference.

The recovered MIR and FIR SED, including the  $< 3\sigma$  (non-) detections at  $100 \mu\text{m}$  and  $160 \mu\text{m}$ , is then modelled with a set of templates of dust grain emission<sup>15</sup> (DL07 dust model), assuming  $q_{\text{PAH}} = 3.19\%$  and  $U_{\text{max}} = 10^6$  (respectively, the fraction of dust mass in polycyclic aromatic hydrocarbon (PAH) grains and the maximum starlight intensity seen by the dust relative to the local interstellar radiation field) but with varying  $\gamma$  and  $U_{\text{min}}$  (respectively, the fraction of dust enclosed in photodissociation regions and the minimum starlight intensity), to estimate the total infrared luminosity  $L_{\text{IR}}$  and dust mass  $M_{\text{dust}}$ . Conversely, the dust temperature  $T_{\text{dust}}$  is determined using a simple modified blackbody model with a varying effective emissivity  $\beta$ , which yields  $\beta = 1.8 \pm 0.3$ . The derived parameter estimates are given in Supplementary Table 2. We note that  $M_{\text{dust}}$  estimates could vary substantially between a simple single-temperature modified blackbody model fit to the data and that of a full dust model such as DL07. However, when the adopted absorption cross-section of the dust distribution ( $\kappa_{\text{abs}}$ ) used in the modified blackbody model is consistent both in the normalization and in the spectral index with that of the full dust model (DL07), the two techniques yield comparable results<sup>48,49</sup>.

The major source of uncertainty in the derivation of  $M_{\text{dust}}$  is the appropriate value of  $\kappa_{\text{abs}}$ , which remains unknown. However, the prescription used in the DL07 model provides  $M_{\text{dust}}$  (and therefore  $M_{\text{gas}}$ ) estimates that are consistent with independent gas measurements of carbon monoxide (CO) excitation in star-forming galaxies at various redshifts<sup>15,50</sup>. Furthermore, the DL07 model has been

used to derive  $M_{\text{gas}}$  estimates for the comparison sample of local quiescent galaxies. Thus, our choice of the DL07 model for our analysis, even if the derived absolute value of  $M_{\text{dust}}$  remains uncertain, facilitates the comparison between various local and high- $z$  samples and avoids any model-dependent systematics.

Finally, we also add to the best-fit DL07 model a power-law radio slope with spectral index  $\alpha = 0.8$  and a normalization given by the FIR–radio correlation<sup>51</sup>. The radio fluxes are, however, not included in the fit, and both the data point and model are shown for reference only. There appears to be a significant excess in the median flux at 1.4 GHz and 3 GHz compared with the model, corresponding to  $\sim 5 \times 10^{22}$  W/Hz. On the one hand, this is suggestive of the presence in our sample of low-excitation AGNs<sup>52</sup> and might be a sign of widespread, persistent AGN feedback. In this case, the duty cycle should be  $f_{\text{BH}} \gtrsim 0.5$ , because the excess is detected in a median stack. A more accurate value can be estimated under the simple assumption that the AGN activity is randomly distributed over the time interval ( $t_{z=1.4} - t_{z=2.5}$ ) probed by our sample, in single bursts of varying duration,  $\Delta t_b$ , and constant luminosity set by the low-redshift radio luminosity functions<sup>52</sup>. For each  $\Delta t_b$ , the radio luminosity is estimated through Monte Carlo simulations by sampling, for each galaxy, the single-burst model at its observed redshift. Varying  $\Delta t_b$  to match the observed excess luminosity then yields  $f_{\text{BH}} = \Delta t_b / (t_{z=1.4} - t_{z=2.5}) \sim 0.66$ . This would imply that the radio AGN is almost always ‘on’ in these galaxies, as opposed to the local Universe where  $f_{\text{BH}} < 0.01$  (ref. 53). The radio spectral index is  $\sim -0.82$ , which is very close to the typical value for star formation emission, but can also be produced by AGN-related processes<sup>54,55</sup>. On the other hand, the normalization of the FIR–radio correlation has a dispersion of a factor of  $\sim 2$  (ref. 56), potentially lowering the significance of this excess, and in local ETGs the 1.4 GHz flux appears to be weakly correlated with FIR luminosity<sup>57</sup>. However, for an entire galaxy population to deviate from the median relation would imply that the slope and normalization of the FIR–radio correlation vary substantially with, for example, SFE or sSFR, which is not substantiated by recent high-redshift studies<sup>51,58,59</sup>.

**Converting  $M_{\text{dust}}$  into  $M_{\text{gas}}$ .** Although  $M_{\text{dust}}$  can be obtained directly from the FIR emission, the molecular gas mass  $M_{\text{gas}}$  is a more important quantity in the context of galaxy evolution. Since molecular hydrogen is essentially invisible,  $M_{\text{gas}}$  is usually extrapolated from other observables, from either submillimetre molecular (for example, CO) line emission or  $M_{\text{dust}}$ , using conversion factors that are uncertain. In the case of  $M_{\text{dust}}$ , a gas-to-dust ratio (G/D) is used, which is related to the gas-phase metallicity and to processes of dust creation and destruction. We use here  $G/D \sim 95$ , based on the parameterization of the G/D as a function of metallicity from Magdis et al.<sup>15</sup> and the assumption of solar metallicity for the gas in the ETGs, which is supported by two lines of indirect evidence: first, the average gas metallicity of star-forming galaxies with the same sSFR is close to (or slightly above) the solar value, up to  $z \sim 1.7$  (refs 60,61); second, a spectroscopic, rest-frame UV measurement of the metallicity of the last batch of stars in a subset of our ETG sample also yields  $\sim Z_{\odot}$  (ref. 19), the stellar metallicity being expected to be slightly lower, but otherwise comparable, to the gas one<sup>62</sup>.

The picture is, however, complicated by processes that can produce dust, such as supernovae, asymptotic giant-branch stars or accretion of gas-phase metals in the ISM, and those that can destroy it (for example, X-ray sputtering<sup>63</sup>). While the bulk of cold dust in local ETGs does not appear to originate from stellar evolution<sup>14,64</sup>, the G/D of ETGs might nonetheless not follow the same relations as MS galaxies. Conversely, in local ETGs that have detected  $\text{H}_2$  gas (the gas-rich population), the median G/D is somewhat higher ( $\sim 400$ ), while in the undetected ones the median upper limit on the G/D is slightly lower ( $\sim 80$ ) than our adopted value<sup>1</sup>. Overall, the global G/D of local ETGs appears to follow a similar relation to that of star-forming galaxies<sup>1,14,65</sup>.

Finally, although knowing the exact state of the gas in our distant ETGs is not necessary for the purposes of this work, we make the simplification that all the hydrogen gas is in molecular ( $\text{H}_2$ ) form, rather than atomic ( $\text{H I}$ ) or a mix of both. We base this assumption on the high average ( $\text{H}_2/\text{H I}$ )  $\sim 2$ – $5$  ratio seen in local ETGs<sup>16,17,66,67</sup>. Moreover, the  $\text{H}_2/\text{H I}$  ratio is expected to increase with redshift and gas column density<sup>70</sup>. This ratio, nevertheless, appears to vary substantially in the local population<sup>71</sup>, possibly as a result of differential evolution, with lenticular (S0) galaxies containing higher amounts of  $\text{H}_2$  (ref. 72). While high-redshift quiescent galaxies tend to have a more disk morphology (that is, closer to S0s) than local ETGs<sup>73–75</sup> (see also Supplementary Section 4), the cold gas in at least some local S0s might have a different origin than that of high-redshift ETGs<sup>76,77</sup>.

**Morphologies.** There exist several publicly available high-resolution imaging datasets on the COSMOS field, taken with the Hubble Space Telescope (HST). The most extensive was obtained with the Advanced Camera for Surveys (ACS) and covers 1.7 deg at 814 nm (ref. 78), corresponding to rest-frame UV wavelengths at  $z > 1.4$ . This implies that HST/ACS imaging might, for this sample, trace the younger stars produced by the last significant star-forming episode more than the total stellar mass distribution. Moreover, the existence of colour gradients in high-redshift ETGs is well attested<sup>79–81</sup>, which implies that their morphological parameters depend on the wavelength at which they are measured. Here, we therefore use the much smaller CANDELS (Cosmic Assembly Near-Infrared Deep Extragalactic Legacy Survey)<sup>82</sup>, which benefits from near-infrared (that is, rest-frame optical) data at

1.2  $\mu\text{m}$  and 1.6  $\mu\text{m}$ . We select the 46 ETGs in our sample whose position overlaps with the HST/WFC3 (Wide-Field Camera 3) mosaics of the CANDELS (a random selection of which is shown in Supplementary Fig. 5), and 12 medium-luminosity stars ( $14 < V < 16$ ) in the same region. We extract cutouts around the targets from both the F125W and F160W images and combine them using the same method as in Supplementary Section 3, to generate median near-infrared images of the galaxies and point sources. These are then used in conjunction with the GALFIT code<sup>83</sup> and fitted with a Sérsic profile. This yields a Sérsic index of  $n = 3.5 \pm 0.1$  and an effective radius of  $r_e = 1.7 \pm 0.1$  kpc, consistent with spheroidal morphology and on the stellar-mass–size relation for ETGs at this redshift<sup>84,85</sup>. The results of this morphological modelling are shown in Supplementary Fig. 6. Furthermore, 40 of these galaxies have individually measured morphologies in the CANDELS catalogue<sup>85</sup>, with median values of  $n \sim 3$  and  $r_e \sim 1.3$  kpc, respectively. Similar results and high Sérsic indices are also found for the full sample; more details will be presented in a future publication. Conversely, in the 3 GHz median image, the ETG stack appears less concentrated, with  $r_e \sim 3.4$  kpc for a fit with a fixed  $n \sim 1$  (exponential) profile. The signal-to-noise ratio of the stacked image is, however, not sufficient for a two-parameter fit. Although  $n \sim 1$  yields a good fit, it is not clear whether this reflects the structure of the galaxies (or parts thereof) or stems from, for example, the averaging over the whole sample of randomly oriented jets.

**Hydrodynamical simulations.** The cosmological simulation used in this work (Fig. 4) is performed in a zoom box focusing on a massive galaxy at the centre of its dark matter halo. The size of the box corresponds to twice the virial radius of the dark halo, without boundary conditions for mass inflow. The latter is based on a large-scale cosmological simulation. The simulation of a forming ETG analysed here is from Martig et al.<sup>8</sup>, with a complete sample presented in Martig et al.<sup>21</sup>. The evolution of the morphology of both its gas and star components is shown in Supplementary Fig. 7. The galaxy starts as disk-dominated at high redshift ( $z > 1.5$ ), then undergoes a series of mergers with mass ratios ranging from 10:1 to 3:1. These mergers have two effects: they convert the stellar structure into a spheroid and compress the gas, increasing the star formation and gas consumption rates. Over the 3 Gyr long track used in Fig. 4, the stellar morphology is consistently spheroidal, although sometimes disturbed by mergers in their early stages. Over this period, the stellar mass increases from  $\sim 6 \times 10^{10} M_{\odot}$  to  $1.2 \times 10^{11} M_{\odot}$ , consistent with our observed sample. About 40% of this increase comes from star formation internal to the studied galaxies, while the rest is accreted during mergers with other, smaller galaxies.

The idealized simulations are performed with the adaptive mesh refinement code RAMSES (ref. 86). They are similar to those presented in Martig et al.<sup>87</sup>, but have double the resolution, reaching 3 pc in the densest gas regions<sup>8</sup>. The gas fraction coverage has been extended with new simulations, fully identical to the previous ones for all other parameters. These idealized simulations do not follow the formation of a given galaxy in a cosmological context. Instead, the stellar and gas mass, as well as their spatial distributions, are arbitrarily chosen to be representative of a certain type of galaxy. The simulations reach a very high resolution to accurately describe the fragmentation of gas in the dense clouds where stars form<sup>87</sup>. They also allow for direct comparisons of the SFE between disk-dominated galaxies and ETGs, with all other parameters being identical. The SFE is determined by the gas surface density, principally, and the rotation curve of the galaxy where the gas is located. In our simulated high-redshift galaxies, the critical value is  $70$ – $100 M_{\odot} \text{pc}^{-2}$  at the half-mass radius of the gas. This then corresponds to gas fraction  $f_{\text{gas}} \sim 25\%$  at high redshift, compared with  $f_{\text{gas}} = 2$ – $3\%$  at  $z \sim 0$ , due to the expected  $\sim 3$ – $4$ -fold increase in the size of gas disks (that is, a factor of 9–16 in surface size) in high-redshift ETGs compared with the compact ones seen in local ETGs<sup>66,76,85</sup>. The error bars in Fig. 4 correspond to the root mean squared fluctuation of the SFE between various snapshots of a given simulation. The agreement between these idealized simulations and the cosmological simulation confirms that the process highlighted in the cosmological simulation is not redshift-dependent: although the reduction of the SFE in a spheroid-dominated galaxy (when enough gas has been consumed) happens at about redshift  $z \sim 1$  in this simulation, it can just as well occur at higher redshift, as in our observations. Finally, the idealized simulations do not include diffuse gas reservoirs in the galaxies’ outskirts, yielding slightly lower gas masses and thus slightly higher values of the SFE than the cosmological simulation.

**Gas and dust return rate.** The amount of gas returned to the ISM by a stellar population depends on both its IMF and the star formation history (SFH). It is generally among the parameters estimated by stellar population synthesis models for single age populations<sup>43,88</sup>. The typical mass-weighted age of BzK-selected quiescent galaxies inferred from spectroscopy is  $t_{\text{SF}} = 2$ – $3$  Gyr (refs 19,89). We assume a delayed, exponentially declining SFH, arbitrarily starting at  $z = 10$ , as the simple parametric form that is closest to the probable ‘true’ SFH of these high-redshift ETGs (rising as the galaxy grows on or above the MS, then decreasing during quenching). In this case, the SFH that would reproduce the SFR inferred from the cold dust emission has  $t_{\text{SF}} \sim 2.24$  Gyr. The amount of gas returned to the ISM over a certain time span can then be computed easily as the convolution of the SFH and mass loss function due to stellar death. For our chosen SFH and IMF, this would amount to  $\sim 4.5 \times 10^{10} M_{\odot}$ , or  $37^{+2}_{-2}\%$  of the observed stellar mass at

$z = 1.76$ , and, given the median stellar mass of ETGs in this sample, an average return rate of  $1.3_{-1.3}^{+1.6} M_{\odot} \text{ yr}^{-1}$  over the last 500 Myr. Similarly, assuming dust yields for solar-metallicity asymptotic giant-branch stars<sup>50</sup>,  $\sim 5 \times 10^8 M_{\odot}$  would have been returned to the ISM, corresponding to  $\sim 1\%$  of the returned gas mass. Single-burst or truncated SFHs, also commonly used in spectral and photometric modelling, would yield similar total gas fractions but negligible return rates at  $z = 1.76$ .

The typical best-fit SFH we infer for these ETGs<sup>19</sup> would produce a large amount of postmain-sequence stars at  $z \sim 1.76$ , which could then contribute substantially to the radiation field to which the dust is exposed. Whether the FIR emission we see is reprocessed radiation from massive, young stars (star formation) or evolved stars then depends on the geometric distribution of the dust, which is unknown. We can, however, estimate the amount of FIR emission produced by non-star-formation sources in a simple case using the class of delayed exponential SFHs mentioned above, truncated for the last 500 Myr so as to have no ongoing star formation. We then use these SFHs to produce composite stellar population models<sup>13</sup>, with which we model the UV–optical SEDs of our ETGs. We assume a standard dust extinction law<sup>91</sup> with a fixed steep slope  $\delta = -0.4$ , typical of low sSFR galaxies, and a UV bump amplitude linearly dependent on  $\delta$  (ref. <sup>92</sup>). In this case, we find that the median difference between the integrated flux of models before and after applying extinction, that is, the maximum luminosity that can arise from evolved stellar populations absorbed by the dust, is  $L_{\text{abs}} = (9 \pm 5) \times 10^9 L_{\odot}$ , or less than half of the measured  $L_{\text{IR}}$ .

Finally, assuming a closed-box evolution to  $z = 0$ , an additional  $\sim 10^{10} M_{\odot}$  of gas and  $\sim 6 \times 10^8 M_{\odot}$  of dust should be produced by stellar evolution, vastly more than currently observed in local ETGs<sup>14</sup>, and highlighting the importance of dust and gas removal mechanisms<sup>7,53,63,93</sup> in the evolution of the ISM of ETGs.

**X-ray stacking.** We use deep X-ray observations of the COSMOS field by the Chandra and XMM-Newton observatories<sup>30,95</sup> to constrain the total mass of the halos hosting our sample ETGs. This procedure is similar to that described in Béthermin et al.<sup>36</sup> and Gobat et al.<sup>36</sup>, and we refer to these articles for additional information. There are 585 sample ETGs in the Chandra COSMOS field and located in zones free from emission. After subtracting both background and point sources, we find a residual flux in the 0.5–2 keV band of  $(2.3 \pm 0.6) \times 10^{-17} \text{ erg cm}^{-2} \text{ s}^{-1}$ , corresponding to an X-ray luminosity of  $L_{\text{X}} = (5.1 \pm 1.3) \times 10^{42} \text{ erg cm}^{-2} \text{ s}^{-1}$  and a mass within  $R_{200c}$  of  $M_{200c} = (1.2 \pm 0.2) \times 10^{13} M_{\odot}$ .

**Data availability.** The data that support the plots within this paper and other findings of this study are available from the corresponding author upon reasonable request.

Received: 6 March 2017; Accepted: 28 November 2017;  
Published online: 15 January 2018

## References

- Lianou, S., Xilouris, E., Madden, S. & Barmby, P. The dustier early-type galaxies deviate from late-type galaxies' scaling relations. *Mon. Not. R. Astron. Soc.* **461**, 2856–2866 (2016).
- Sargent, M. T. et al. A direct constraint on the gas content of a massive, passively evolving elliptical galaxy at  $z = 1.43$ . *Astrophys. J. Lett.* **806**, 6 (2015).
- Gobat, R. et al. The early early type: discovery of a passive galaxy at  $z_{\text{spec}} \sim 3$ . *Astrophys. J. Lett.* **759**, 5 (2012).
- Glazebrook, K. et al. A massive, quiescent galaxy at redshift of  $z = 3.717$ . *Nature* **544**, 71–74 (2017).
- Di Matteo, T., Springel, V. & Hernquist, L. Energy input from quasars regulates the growth and activity of black holes and their host galaxies. *Nature* **433**, 604–607 (2005).
- Birnboim, Y. & Dekel, A. Virial shocks in galactic haloes? *Mon. Not. R. Astron. Soc.* **345**, 349–364 (2003).
- Croton, D. J. et al. The many lives of active galactic nuclei: cooling flows, black holes and the luminosities and colours of galaxies. *Mon. Not. R. Astron. Soc.* **365**, 11–28 (2006).
- Martig, M., Bournaud, F., Teyssier, R. & Dekel, A. Morphological quenching of star formation: making early-type galaxies red. *Astrophys. J.* **707**, 250–267 (2009).
- Tacchella, S. et al. Evidence for mature bulges and an inside-out quenching phase 3 billion years after the Big Bang. *Science* **348**, 314–317 (2015).
- Daddi, E. et al. A new photometric technique for the joint selection of star-forming and passive galaxies at  $1.4 \lesssim z \lesssim 2.5$ . *Astrophys. J.* **617**, 746–764 (2004).
- Wuyts, S. et al. What do we learn from IRAC observations of galaxies at  $2 < z < 3.5$ ? *Astrophys. J.* **655**, 51–65 (2007).
- Draine, B. T. & Li, A. Infrared emission from interstellar dust. IV. The silicate-graphite-PAH model in the post-Spitzer era. *Astrophys. J.* **657**, 810–837 (2007).
- Hwang, H. S. et al. Evolution of dust temperature of galaxies through cosmic time as seen by Herschel. *Mon. Not. R. Astron. Soc.* **409**, 75–82 (2010).
- Smith, M. W. et al. The Herschel reference survey: dust in early-type galaxies and across the Hubble sequence. *Astrophys. J.* **748**, 25 (2012).
- Magdis, G. et al. The evolving interstellar medium of star-forming galaxies since  $z = 2$  as probed by their infrared spectral energy distributions. *Astrophys. J.* **760**, 23 (2012).
- Young, L. M. et al. The ATLAS<sup>3D</sup> project—IV. The molecular gas content of early-type galaxies. *Mon. Not. R. Astron. Soc.* **414**, 940–967 (2011).
- Young, L. M. et al. The ATLAS<sup>3D</sup> project—XXVII. Cold gas and the colours and ages of early-type galaxies. *Mon. Not. R. Astron. Soc.* **444**, 3408–3426 (2014).
- Kennicutt, R. C. Star formation in galaxies along the Hubble sequence. *Annu. Rev. Astron. Astrophys.* **36**, 189–231 (1998).
- Gobat, R. et al. In and out star formation in  $z \sim 1.5$  quiescent galaxies from rest-frame UV spectroscopy and the far-infrared. *Astron. Astrophys.* **599**, 12 (2017).
- Saintonge, A. et al. The impact of interactions, bars, bulges, and active galactic nuclei on star formation efficiency in local massive galaxies. *Astrophys. J.* **758**, 17 (2012).
- Martig, M., Bournaud, F., Croton, D. J., Dekel, A. & Teyssier, R. A diversity of progenitors and histories for isolated spiral galaxies. *Astrophys. J.* **756**, 29 (2012).
- Johansson, P. H., Naab, T. & Ostriker, J. P. Gravitational heating helps make massive galaxies red and dead. *Astrophys. J. Lett.* **697**, L38–L43 (2009).
- Salpeter, E. E. The luminosity function and stellar evolution. *Astrophys. J.* **121**, 161–166 (1955).
- Grillo, C. & Gobat, R. On the initial mass function and tilt of the fundamental plane of massive early-type galaxies. *Mon. Not. R. Astron. Soc. Lett.* **402**, 67–71 (2010).
- Cappellari, M. et al. Systematic variation of the stellar initial mass function in early-type galaxies. *Nature* **484**, 485–488 (2012).
- Conroy, C. & van Dokkum, P. G. The stellar initial mass function in early-type galaxies from absorption line spectroscopy. II. Results. *Astrophys. J.* **760**, 16 (2012).
- Larson, D. et al. Seven-year Wilkinson microwave anisotropy probe (WMAP) observations: power spectra and WMAP-derived parameters. *Astrophys. J. Suppl. S.* **192**, 19 (2011).
- Planck Collaboration et al. Planck 2015 results. XIII. Cosmological parameters. *Astron. Astrophys.* **594**, 63 (2015).
- Scoville, N. et al. The Cosmic Evolution Survey (COSMOS): overview. *Astrophys. J. Suppl. S.* **172**, 1–8 (2007).
- McCracken, H. J. et al. The COSMOS-WIRCam near-infrared imaging survey. I. BzK-selected passive and star-forming galaxy candidates at  $z \gtrsim 1.4$ . *Astrophys. J.* **708**, 202–217 (2010).
- Muzzin, A. et al. A public K<sub>s</sub>-selected catalog in the COSMOS/UltraVISTA field: photometry, photometric redshifts, and stellar population parameters. *Astrophys. J. Suppl. S.* **206**, 19 (2013).
- Le Floch, E. et al. Deep Spitzer 24  $\mu\text{m}$  COSMOS imaging. I. The evolution of luminous dusty galaxies—confronting the models. *Astrophys. J.* **703**, 222–239 (2009).
- Lilly, S. J. et al. zCOSMOS: a large VLT/VIMOS redshift survey covering  $0 < z < 3$  in the COSMOS field. *Astrophys. J. Suppl. S.* **172**, 70–85 (2007).
- Strazzullo, V. et al. Passive galaxies as tracers of cluster environments at  $z \sim 2$ . *Astron. Astrophys.* **576**, 5 (2015).
- Williams, R. J., Quadri, R. F., Franx, M., van Dokkum, P. & Labbé, I. Detection of quiescent galaxies in a bicolor sequence from  $z = 0–2$ . *Astrophys. J.* **691**, 1879–1895 (2009).
- Gobat, R. et al. Retal Satellite content and quenching of star formation in galaxy groups at  $z \sim 1.8$ . *Astron. Astrophys.* **581**, 12 (2015).
- Lutz, D. et al. PACS Evolutionary Probe (PEP)—a Herschel key program. *Astron. Astrophys.* **532**, 12 (2011).
- Oliver, S. J. et al. The Herschel Multi-tiered Extragalactic Survey: HerMES. *Mon. Not. R. Astron. Soc.* **424**, 1614–1635 (2012).
- Geach, J. E. et al. The SCUBA-2 cosmology legacy survey: 850  $\mu\text{m}$  maps, catalogues and number counts. *Mon. Not. R. Astron. Soc.* **465**, 1789–1806 (2017).
- Aretxaga, I. et al. AzTEC millimetre survey of the COSMOS field—III. Source catalogue over  $0.72 \text{ deg}^2$  and plausible boosting by large-scale structure. *Mon. Not. R. Astron. Soc.* **415**, 3831–3850 (2011).
- Smolčić, V. et al. The VLA-COSMOS 3 GHz large project: continuum data and source catalog release. *Astron. Astrophys.* **602**, 19 (2017).
- Schinnerer, E. et al. The VLA-COSMOS survey. IV. Deep data and joint catalog. *Astrophys. J. Suppl. S.* **188**, 384–404 (2010).
- Bruzual, G. & Charlot, S. Stellar population synthesis at the resolution of 2003. *Mon. Not. R. Astron. Soc.* **344**, 1000–1028 (2003).
- Calzetti, D. et al. The dust content and opacity of actively star-forming galaxies. *Astrophys. J.* **533**, 682–695 (2000).

45. Béthermin, M. et al. Evolution of the dust emission of massive galaxies up to  $z = 4$  and constraints on their dominant mode of star formation. *Astron. Astrophys.* **573**, 17 (2015).
46. Man, A. W. S. et al. Confirming the existence of a quiescent galaxy population out to  $z = 3$ : a stacking analysis of mid-, far-infrared and radio data. *Astrophys. J.* **820**, 14 (2016).
47. Viero, M. P. et al. HerMES: the contribution to the cosmic infrared background from galaxies selected by mass and redshift. *Astrophys. J.* **779**, 23 (2013).
48. Bianchi, S. Vindicating single- $T$  modified blackbody fits to Herschel SEDs. *Astron. Astrophys.* **552**, 5 (2013).
49. Berta, S., Lutz, D., Genzel, R., Förster-Schreiber, N. M. & Tacconi, L. J. Measures of galaxy dust and gas mass with Herschel photometry and prospects for ALMA. *Astron. Astrophys.* **587**, 26 (2016).
50. Genzel, R. et al. Combined CO and dust scaling relations of depletion time and molecular gas fractions with cosmic time, specific star-formation rate, and stellar mass. *Astrophys. J.* **800**, 25 (2015).
51. Magnelli, B. et al. The far-infrared/radio correlation and radio spectral index of galaxies in the SFR- $M_*$  plane up to  $z \sim 2$ . *Astron. Astrophys.* **573**, 18 (2015).
52. Best, P. N. & Heckman, T. M. On the fundamental dichotomy in the local radio-AGN population: accretion, evolution and host galaxy properties. *Mon. Not. R. Astron. Soc.* **421**, 1569–1582 (2012).
53. Ciotti, L. & Ostriker, J. P. Cooling flows and quasars. II. Detailed models of feedback-modulated accretion flows. *Astrophys. J.* **551**, 131–152 (2001).
54. O’Dea, C. P. The compact steep-spectrum and gigahertz peaked-spectrum radio sources. *Publ. Astron. Soc. Pac.* **110**, 493–532 (1998).
55. Richards, G. T. et al. Spectral energy distributions and multiwavelength selection of type 1 quasars. *Astrophys. J. Suppl. S.* **166**, 470–497 (2006).
56. Yun, M. S., Reddi, N. A. & Condon, J. J. Radio properties of infrared-selected galaxies in the IRAS 2Jy sample. *Astrophys. J.* **554**, 803–822 (2001).
57. Nyland, K. et al. Star formation in nearby early-type galaxies: the radio continuum perspective. *Mon. Not. R. Astron. Soc.* **464**, 1029–1064 (2017).
58. Ibar, E. Deep multi-frequency radio imaging in the Lockman Hole using the GMRT and VLA—I. The nature of the sub-mJy radio population. *Mon. Not. R. Astron. Soc.* **397**, 281–298 (2009).
59. Thomson, A. P. et al. An ALMA survey of submillimetre galaxies in the Extended Chandra Deep Field South: radio properties and the far-infrared/radio correlation. *Mon. Not. R. Astron. Soc.* **442**, 577–588 (2014).
60. Mannucci, F., Cresci, G., Maiolino, R., Marconi, A. & Gnerucci, A. A fundamental relation between mass, star formation rate and metallicity in local and high-redshift galaxies. *Mon. Not. R. Astron. Soc.* **408**, 2115–2127 (2010).
61. Kashino, D. et al. The FMOS-COSMOS survey of star-forming galaxies at  $z \sim 1.6$ . IV. excitation state and chemical enrichment of the interstellar medium. *Astrophys. J.* **835**, 27 (2017).
62. Halliday, C. et al. GMASS ultradeep spectroscopy of galaxies at  $z \sim 2$ . I. The stellar metallicity. *Astron. Astrophys.* **479**, 417–425 (2008).
63. Arimoto, N., Matsushita, K., Ishimaru, Y., Ohashi, T. & Renzini, A. The iron discrepancy in elliptical galaxies after ASCA. *Astrophys. J.* **477**, 128–143 (1997).
64. Agius, N. K. et al. GAMA/H-ATLAS: linking the properties of submm detected and undetected early-type galaxies—I.  $z \leq 0.06$  sample. *Mon. Not. R. Astron. Soc.* **431**, 1929–1946 (2013).
65. Leeuw, L. L., Davidson, J., Dowell, C. D. & Matthews, H. E. Spatially resolved imaging at 350  $\mu\text{m}$  of cold dust in nearby elliptical galaxies. *Astrophys. J. Lett.* **677**, 249–261 (2008).
66. Crocker, A. F., Bureau, M., Young, L. M. & Combes, F. Molecular gas and star formation in early-type galaxies. *Mon. Not. R. Astron. Soc.* **410**, 1197–1222 (2011).
67. Davis, T. A. et al. Molecular and atomic gas in dust lane early-type galaxies—I. Low star formation efficiencies in minor merger remnants. *Mon. Not. R. Astron. Soc.* **449**, 3503–3516 (2015).
68. Lagos, C. D. P. et al. Cosmic evolution of the atomic and molecular gas contents of galaxies. *Mon. Not. R. Astron. Soc.* **418**, 1649–1667 (2011).
69. Lagos, C. D. P. et al. Which galaxies dominate the neutral gas content of the Universe? *Mon. Not. R. Astron. Soc.* **440**, 920–941 (2014).
70. Sternberg, A., Le Petit, F., Roueff, E. & Le Bourlot, J. H<sub>1</sub>-to-H<sub>2</sub> transitions and H<sub>1</sub> column densities in galaxy star-forming regions. *Astrophys. J.* **790**, 30 (2014).
71. Welch, G. A., Sage, L. J. & Young, L. M. The cool interstellar medium in elliptical galaxies. II. Gas content in the volume-limited sample and results from the combined elliptical and lenticular surveys. *Astrophys. J.* **725**, 100–114 (2010).
72. Sage, L. J., Welch, G. A. & Young, L. M. The cool ISM in elliptical galaxies. I. A survey of molecular gas. *Astrophys. J.* **657**, 232–240 (2007).
73. Chevance, M. et al. On the shapes and structures of high-redshift compact galaxies. *Astrophys. J. Lett.* **754**, 5 (2012).
74. Krogager, J.-K., Zirm, A. W., Toft, S., Man, A. & Brammer, G. A spectroscopic sample of massive, quiescent  $z \sim 2$  galaxies: implications for the evolution of the mass–size relation. *Astrophys. J.* **797**, 14 (2014).
75. Bruce, V. A. et al. The bulge-disc decomposed evolution of massive galaxies at  $1 < z < 3$  in CANDELS. *Mon. Not. R. Astron. Soc.* **444**, 1001–1033 (2014).
76. Davis, T. A. et al. The ATLAS<sup>3D</sup> project—X. On the origin of the molecular and ionized gas in early-type galaxies. *Mon. Not. R. Astron. Soc.* **417**, 882–899 (2011).
77. Katkov, I. Y., Silchenko, O. K. & Afanasiev, V. L. Decoupled gas kinematics in isolated S0 galaxies. *Mon. Not. R. Astron. Soc.* **438**, 2798–2803 (2014).
78. Koekemoer, A. M. et al. The COSMOS survey: Hubble Space Telescope Advanced Camera for Surveys observations and data processing. *Astrophys. J. Suppl. S.* **172**, 196–202 (2007).
79. Guo, Y. et al. Color and stellar population gradients of passively evolving galaxies at  $z \sim 2$  from HST/WFC3 deep imaging in the Hubble ultra deep field. *Astrophys. J.* **735**, 17 (2011).
80. Gargiulo, A., Saracco, P., Longhetti, M., La Barbera, F. & Tamburri, S. Spatially resolved colours and stellar population properties in early-type galaxies at  $z \sim 1.5$ . *Mon. Not. R. Astron. Soc.* **425**, 2698–2714 (2012).
81. Chan, J. C. C. et al. Sizes, colours gradients and resolved stellar mass distributions for the massive cluster galaxies in XMMUJ2235–2557 at  $z = 1.39$ . *Mon. Not. R. Astron. Soc.* **458**, 3181–3209 (2016).
82. Koekemoer, A. M. et al. CANDELS: The Cosmic Assembly Near-Infrared Deep Extragalactic Legacy Survey—the Hubble Space Telescope observations, imaging data products, and mosaics. *Astrophys. J. Suppl. S.* **197**, 36 (2011).
83. Peng, C. Y., Ho, L. C., Impey, C. D. & Rix, H.-W. Detailed decomposition of galaxy images. II. Beyond axisymmetric models. *Astron. J.* **139**, 2097–2129 (2010).
84. Mancini, C. et al. High-redshift elliptical galaxies: are they (all) really compact? *Mon. Not. R. Astron. Soc.* **401**, 933–940 (2010).
85. van der Wel, A. et al. 3d-HST + CANDELS: The evolution of the galaxy size–mass distribution since  $z = 3$ . *Astrophys. J.* **788**, 19 (2014).
86. Teysseier, R. Cosmological hydrodynamics with adaptive mesh refinement. A new high resolution code called RAMSES. *Astron. Astrophys.* **385**, 337–364 (2002).
87. Martig, M. et al. The ATLAS<sup>3D</sup> project—XXII. Low-efficiency star formation in early-type galaxies: hydrodynamic models and observations. *Mon. Not. R. Astron. Soc.* **432**, 1914–1927 (2013).
88. Maraston, C. Evolutionary population synthesis: models, analysis of the ingredients and application to high- $z$  galaxies. *Mon. Not. R. Astron. Soc.* **362**, 799–825 (2005).
89. Onodera, M. et al. The ages, metallicities, and element abundance ratios of massive quenched galaxies at  $z \geq 1.6$ . *Astrophys. J.* **808**, 12 (2015).
90. Ventura, P. et al. Dust from asymptotic giant branch stars: relevant factors and modelling uncertainties. *Mon. Not. R. Astron. Soc.* **439**, 977–989 (2014).
91. Noll, S. et al. GMASS ultradeep spectroscopy of galaxies at  $z \sim 2$ . IV. The variety of dust populations. *Astron. Astrophys.* **499**, 69–85 (2009).
92. Kriek, M. & Conroy, C. The dust attenuation law in distant galaxies: evidence for variation with spectral type. *Astrophys. J. Lett.* **775**, 6 (2013).
93. Ciotti, L., D’Ercole, A., Pellegrini, S. & Renzini, A. Winds, outflows, and inflows in X-ray elliptical galaxies. *Astrophys. J.* **376**, 380–403 (1991).
94. Finoguenov, A. et al. The XMM-Newton wide-field survey in the COSMOS field: statistical properties of clusters of galaxies. *Astrophys. J. Suppl. S.* **172**, 128–195 (2007).
95. Elvis, M. et al. The Chandra COSMOS survey. I. Overview and point source catalog. *Astrophys. J. Suppl. S.* **184**, 158–171 (2009).
96. Béthermin, M. et al. Clustering, host halos, and environment of  $z \sim 2$  galaxies as a function of their physical properties. *Astron. Astrophys.* **567**, 17 (2014).
97. Leroy, A. K. The star formation efficiency in nearby galaxies: measuring where gas forms stars effectively. *Astron. J.* **136**, 2782–2845 (2008).
98. Saintonge, A. et al. COLD GASS, an IRAM legacy survey of molecular gas in massive galaxies—I. Relations between H<sub>2</sub>, H<sub>1</sub>, stellar content and structural properties. *Mon. Not. R. Astron. Soc.* **415**, 32–60 (2011).
99. Bauermeister, A. et al. The EGN0g survey: molecular gas in intermediate-redshift star-forming galaxies. *Astrophys. J.* **768**, 27 (2013).
100. Geach, J. E. et al. On the evolution of the molecular gas fraction of star-forming galaxies. *Astrophys. J. Lett.* **730**, 5 (2011).
101. Daddi, E. et al. Different star formation laws for disks versus starbursts at low and high redshifts. *Astrophys. J. Lett.* **714**, L118–L122 (2010).
102. Tacconi, L. J. et al. PHIBSS: molecular gas content and scaling relations in  $z \sim 1–3$  massive, main-sequence star-forming galaxies. *Astrophys. J.* **768**, 22 (2013).
103. Boselli, A. et al. Cold gas properties of the Herschel reference survey. II. Molecular and total gas scaling relations. *Astron. Astrophys.* **564**, 18 (2014).

104. Sargent, M. T. et al. Regularity underlying complexity: a redshift-independent description of the continuous variation of galaxy-scale molecular gas properties in the mass-star formation rate plane. *Astrophys. J.* **793**, 34 (2014).
105. Davis, T. A. et al. The ATLAS<sup>3D</sup> project—XXVIII. Dynamically driven star formation suppression in early-type galaxies. *Mon. Not. R. Astron. Soc.* **444**, 3427–3445 (2014).

### Acknowledgements

The authors thank S. Lianou for providing models of dust emission in local ETGs and V. Smolčić for the 3 GHz radio data. S.J. acknowledges China Scholarship Council funding. The new simulations presented in this work were performed on GENCI resources (allocations 2016-04-2019 and 2017-04-2192).

### Author contributions

R.G. and E.D. devised the project. R.G. analysed the data and wrote the manuscript. G.M. modelled the FIR emission. F.B. and M.M. carried out and analysed the

simulations. M.S. and M.B. provided some of the theoretical framework. S.J. provided the MIR catalogue. A.F. analysed the X-ray observations. G.W.W., I.A. and M.Y. provided submillimetre data. H.S.H., A.R., V.S. and E.V. provided critical feedback that helped shape the manuscript.

### Competing interests

The authors declare no competing financial interests.

### Additional information

**Supplementary information** is available for this paper at <https://doi.org/10.1038/s41550-017-0352-5>.

**Reprints and permissions information** is available at [www.nature.com/reprints](http://www.nature.com/reprints).

**Correspondence and requests for materials** should be addressed to R.G.

**Publisher's note:** Springer Nature remains neutral with regard to jurisdictional claims in published maps and institutional affiliations.